Title
Exchange-Interaction-Like Behavior in Ferroelectric Bilayers

Journal
Advanced Materials, 35(39)

ISSN
0935-9648

Authors
Kavle, Pravin
Ross, Aiden M
Zorn, Jacob A
et al.

Publication Date
2023-09-01

DOI
10.1002/adma.202301934

ADVANCED MATERIALS
www.advmat.de

Exchange-Interaction-Like Behavior in Ferroelectric Bilayers

Pravin Kavle, Aiden M. Ross, Jacob A. Zorn, Piush Behera, Eric Parsonnet, Xiaoxi Huang, Ching-Che Lin, Lucas Caretta, Long-Qing Chen, and Lane W. Martin**

Interlayer coupling in materials, such as exchange interactions at the interface between an antiferromagnet and a ferromagnet, can produce exotic phenomena not present in the parent materials. While such interfacial coupling in magnetic systems is widely studied, there is considerably less work on analogous electric counterparts (i.e., akin to electric "exchange-bias-like" or "exchange-spring-like" interactions between two polar materials) despite the likelihood that such effects can also engender new features associated with anisotropic electric dipole alignment. Here, electric analogs of such exchange interactions are reported, and their physical origins are explained for bilayers of in-plane polarized $Pb_{1-x}Sr_xTiO_3$ ferroelectrics. Variation of the strontium content and thickness of the layers provides for deterministic control over the switching properties of the bilayer system resulting in phenomena analogous to an exchange-spring interaction and, leveraging added control of these interactions with an electric field, the ability to realize multistate-memory function. Such observations not only hold technological promise for ferroelectrics and multiferroics but also extend the similarities between ferromagnetic and ferroelectric materials to include the manifestation of exchange-interaction-like phenomena.

1. Introduction

Coupling across interfaces is important for many fields, such as hydrodynamic coupling across fluid interfaces,[1,2] coupling across interfaces in composite materials with layers having different mechanical properties,[3,4] magnetoelectric coupling in heterostructures consisting of magnetic and piezoelectric materials,[5,6] and exchange interactions at interfaces between ferromagnets and antiferromagnets.[7] Among these, the interface coupling phenomena in multilayer magnetic systems, wherein there can be strong interactions between a ferromagnet and an adjacent ferromagnetic or antiferromagnetic layer, have been widely studied and utilized.[8] Exchange bias (or exchange anisotropy), in particular, is one of the most extensively studied phenomena.[9,10] It describes the situation wherein the magnetic response of a ferromagnetic layer is shifted away from zero magnetic field, resulting from an exchange interaction with an adjacent antiferromagnet layer.[8] This effect was essential for realizing devices such as magnetic read–write heads[11] and magnetic random access memory.[12] Other related phenomena include exchange-spring magnets (ESM) which are achieved by coupling hard and soft ferromagnets such that the hard magnet provides high anisotropy and coercive fields, while the soft magnet enhances the magnetic moment.[13] In such exchange springs, the soft magnet rotates back into alignment with the hard magnet when the applied field is removed; hence the analogy to a spring. The possibility of designing synthetic magnets for specific applications is, thus, intimately related to the ability to induce and tune the couplings between the individual magnetic layers.

On the other hand, considerably less work has been done on anisotropic dipole interactions across the interface between

P. Kavle, P. Behera, X. Huang, C.-C. Lin, L. W. Martin
Department of Materials Science and Engineering
University of California
Berkeley and Materials Sciences Division
Lawrence Berkeley National Laboratory
Berkeley, CA 94720, USA
E-mail: lwmartin@berkeley.edu

A. M. Ross, J. A. Zorn, L.-Q. Chen
Department of Materials Science and Engineering
The Pennsylvania State University
University Park, PA 16802, USA
E-mail: lqc3@psu.edu

E. Parsonnet
Department of Physics
University of California
Berkeley, CA 94720, USA

L. Caretta
Department of Materials Science and Engineering
University of California
Berkeley, CA 94720, USA

P. Kavle, P. Behera, X. Huang, C.-C. Lin, L. Caretta, L. W. Martin
Materials Sciences Division
Lawrence Berkeley National Laboratory
Berkeley, CA 94720, USA

L. Caretta
School of Engineering
Brown University
Providence, RI 02912, USA

The ORCID identification number(s) for the author(s) of this article can be found under https://doi.org/10.1002/adma.202301934

DOI: 10.1002/adma.202301934

different ferroelectric materials and the range of resulting ferroelectric responses that are possible are still not fully explored and understood. It should be noted, of course, that an exchange interaction (in the rigorous sense as defined in magnetic systems) is not possible in ferroelectrics, but analogous coupling between layers via dipolar (electrostatic and potentially elastic) interactions could arise. This said, effects that appear similar to "exchange bias" have been observed in ferroelectrics in the form of hysteresis loops that are shifted along the electric field (voltage) axis due to the presence of an "internal bias field".[14] In general, however, such effects are not due to interfacial coupling but instead can arise for many reasons. For example, it is not uncommon to have preferentially aligned defect dipoles that pin the polarization of the ferroelectric in a given direction, effectively biasing the loop in one direction.[15–18] Compositional (or strain) gradients across the material can also produce similar effects[19,20] due to voltage offsets induced by flexoelectric coupling between the polarization and strain gradient.[21,22] The observed hysteresis loops[20] are similar to that of a soft ferromagnet in an ESM system.[13] Beyond these examples, there are other features that can give rise to built-in bias fields in ferroelectrics, including the presence of asymmetric electrodes[23] wherein different work functions produce asymmetric band bending at different interfaces, interfacial Schottky effects caused by polarization-dependent band bending,[24] charge trapping at electrode interfaces,[25] and surface polar absorbates[26] leading to preferential polarization pinning. A recent study of $BaTiO_3/PrScO_3$ $(110)_O$ heterostructures also showed anisotropic (shifted) ferroelectric hysteresis loops arising from anisotropic strain, monoclinic distortions induced by interfacial oxygen octahedral coupling, and interfacial electrostatic potential stabilized, single-variant in-plane polarized $BaTiO_3$.[27] Finally, "exchange-spring-like" effects have been studied via phase-field approaches in ferroelectric $BaTiO_3$-dielectric $SrTiO_3$ superlattices wherein constricted hysteresis loops due to dipole–dipole interactions have been observed.[28] For these instances, the analogy to magnetic exchange interactions (which is based on cross-interface coupling) does not extend very far. Researchers have, however, also explored multilayer ferroelectric heterostructures in an attempt to manipulate their properties. For example, in bilayers based on the $PbZr_xTi_{1-x}O_3$ system, structures composed of tetragonal $x = 0.3$ and rhombohedral $x = 0.7$ layers showed enhanced piezoelectric behavior due to increased ferroelastic-domain activity[29] and deterministic reorientation of ferroelastic domain walls.[30] Bilayers formed from tetragonal $x = 0.2$ and $x = 0.8$ layers exhibited tunable structural, dielectric, and ferroelectric properties upon altering the order of the films.[19] Such examples demonstrate the potential for coupling ferroelectric layers across interfaces but fall short of observations that are truly analogous to exchange bias or exchange-spring effects. This begs the question of whether such interface-related phenomena observed in magnetism can be realized and tuned in ferroelectric–ferroelectric thin films multilayers?

With consideration to interface-controlled effects, in-plane ferroelectrics could provide a unique opportunity wherein the polarization lies parallel to the substrate surface. For $Pb_{1-x}Sr_xTiO_3$, prior work has illustrated the range of in-plane domain structures that can be produced in this system, including the formation of in-plane ferroelectric superdomains[31] and the field-induced dynamics of which have been explored using an automated experimental approach (FerroBOT[32]).[33] Similar in-plane domains in the $BaTiO_3$ system have been studied for their high-speed collective switching velocities.[34] Here, we demonstrate purely in-plane polarized bilayer ferroelectric heterostructures based on $Pb_{1-x}Sr_xTiO_3$[35] grown on $DyScO_3$ (110) substrates where it is possible to realize phenomena analogous to magnetic exchange-bias and exchange-spring effects in a purely polar system. This is achieved by deterministic control of the coercive field of the individual layers by controlling both the strontium content and the thickness of the individual layers to induce "hard" (high coercivity) and "soft" (low coercivity) versions of the material. In turn, an array of interlayer lattice-polarization couplings are observed, including exchange-spring-like function and ferroelectric bias, which is further tunable via the application of electric fields, such that it is possible to create stable multistate switching in the in-plane direction. Such observations not only hold technological promise for ferroelectric and multiferroic devices but also extend the similarities between ferromagnetic and ferroelectric materials to include the manifestation of exchange-interaction-like phenomena.

2. Results and Discussion

To study the potential for interlayer coupling phenomena, a model system that provides the right combination of properties is required. Here, a compositional series of 100-nm-thick $Pb_{1-x}Sr_xTiO_3$ thin films with $x = 0.4$, 0.6, and 0.8 was synthesized on $DyScO_3$ (110) substrates via pulsed-laser deposition (Experimental Section). Following the growth, structural studies were completed via X-ray diffraction (Figure S1, Supporting Information, Experimental Section) to probe the evolution of the crystal structure of the $Pb_{1-x}Sr_xTiO_3$ films (**Figure 1**a). High-quality, fully epitaxial solid-solution films were obtained for all compositions studied herein. In all cases, the $Pb_{1-x}Sr_xTiO_3$ 200-diffraction peaks appear to shift to higher 2θ values with increasing strontium content (corresponding to a reduction of the out-of-plane lattice parameter). This is consistent with what is expected for the isovalent substitution of a smaller-sized Sr^{2+} cation (144 pm) at the Pb^{2+} cation (149 pm) site.

Further details about the materials, including the domain structure, can be obtained by exploring various features in X-ray reciprocal space mapping (RSM) studies (Experimental Section). Here, considering the observation of only the $Pb_{1-x}Sr_xTiO_3$ 200-diffraction peak, asymmetric RSM studies about the $Pb_{1-x}Sr_xTiO_3$ 310-diffraction condition were completed for all films (Figure S2a, Supporting Information). The asymmetric RSM studies (Figure 1b–d) reveal a film peak corresponding to the 310-diffraction condition of the in-plane polarized domains that have the same Q_x as the $DyScO_3$ 332_O-diffraction peak indicating that the $Pb_{1-x}Sr_xTiO_3$ films grow coherently strained with the underlying substrate. Also, distinct ordering peaks are visible along the [h00] and at the same Q_z position for all $Pb_{1-x}Sr_xTiO_3$ thin films. For example, in the case of $Pb_{0.6}Sr_{0.4}TiO_3$ (Figure 1d), such peaks indicate the systematic long-range ordering of stripe-like, in-plane domains with a periodicity of ≈55 nm. Further asymmetric RSM studies were done about the $Pb_{1-x}Sr_xTiO_3$ $30\bar{1}$-diffraction condition (Figure S2a,b, Supporting Information) to confirm that similar periodicity exists in the other perpendicular

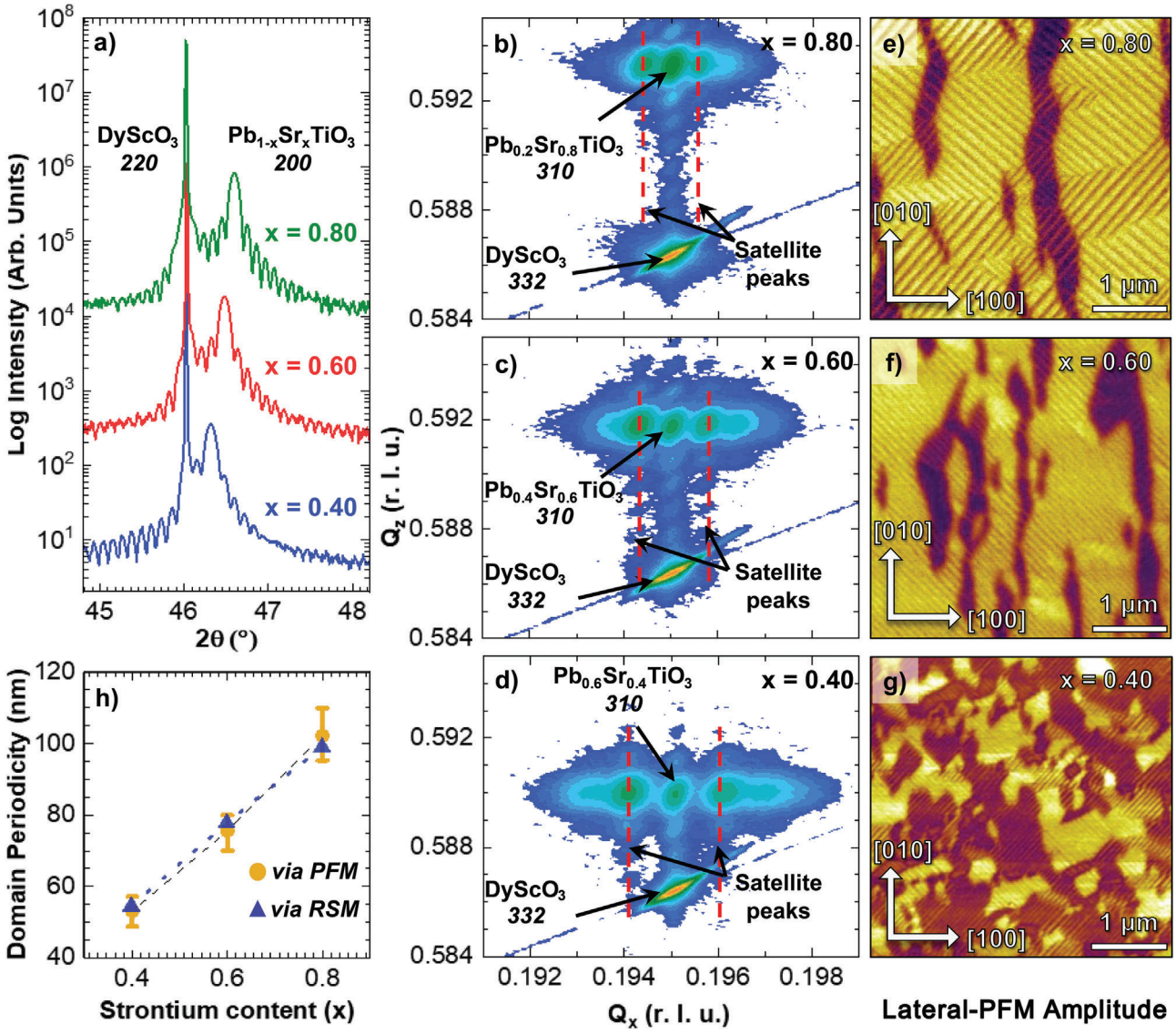

Figure 1. a) θ–2θ X-ray diffraction scans for 100-nm-thick $Pb_{1-x}Sr_xTiO_3$ thin films grown on $DyScO_3$ (110) substrate. From top to bottom, $Pb_{0.2}Sr_{0.8}TiO_3$ (green), $Pb_{0.4}Sr_{0.6}TiO_3$ (red), and $Pb_{0.6}Sr_{0.4}TiO_3$ (blue). 2D RSM about the 332_o-diffraction peak of $DyScO_3$ (110) with a pair of vertical dashed red lines representing domain periodicity satellite peaks for the 100-nm-thick b) $Pb_{0.2}Sr_{0.8}TiO_3$, c) $Pb_{0.4}Sr_{0.6}TiO_3$ and, d) $Pb_{0.6}Sr_{0.4}TiO_3$. Corresponding lateral PFM (L-PFM) images of 100 nm-thick e) $Pb_{0.2}Sr_{0.8}TiO_3$, f) $Pb_{0.4}Sr_{0.6}TiO_3$, and g) $Pb_{0.6}Sr_{0.4}TiO_3$. h) Domain periodicity extracted from 2D-RSM and L-PFM for each composition shows a good match.

direction. Also, RSM studies about the symmetric 200-diffraction condition of the $Pb_{1-x}Sr_xTiO_3$ (Figure S2c, Supporting Information) demonstrate no signature of any satellite peaks, which are usually induced by any regular out-of-plane polarization arrangements associated with the periodic domains.[36] The two possible uncharged domain structures with these types of walls are: i) the aa_1/aa_2 phase wherein the polarization is along the base diagonals of the $Pb_{1-x}Sr_xTiO_3$ unit cell (Figure S3a, Supporting Information) and ii) the a phase (Figure S3b, Supporting Information) with the polarization along the longer base edges of the $Pb_{1-x}Sr_xTiO_3$ unit cell (also called a_1/a_2 or 90° domains).

To further understand the in-plane domain configuration, it is directly visualized via piezoresponse force microscopy (PFM) which, for an entirely in-plane polarized ferroelectric material is detected by lateral PFM (L-PFM).[37] Indeed, in-plane domains are observed in the as-grown films (Figure 1e–g). The orientation of the domain walls along the [110] and [$\bar{1}$10] is consistent with an a_1/a_2-domain structure.[38] Furthermore, the as-grown $Pb_{1-x}Sr_xTiO_3$ films show no other surface features other than substrate terraces (Figure S4a, Supporting Information) and there is no contrast in vertical PFM (Figure S4b, Supporting Information); further supporting the conclusion that the films are fully in-plane polarized. The periodicity of the domain structure, as measured from L-PFM (λ_{PFM}) matches well with the periodicity extracted from the ordering peaks (λ_{RSM}) in the RSM studies (Figure 1h; Figure S5a,b, Supporting Information). An

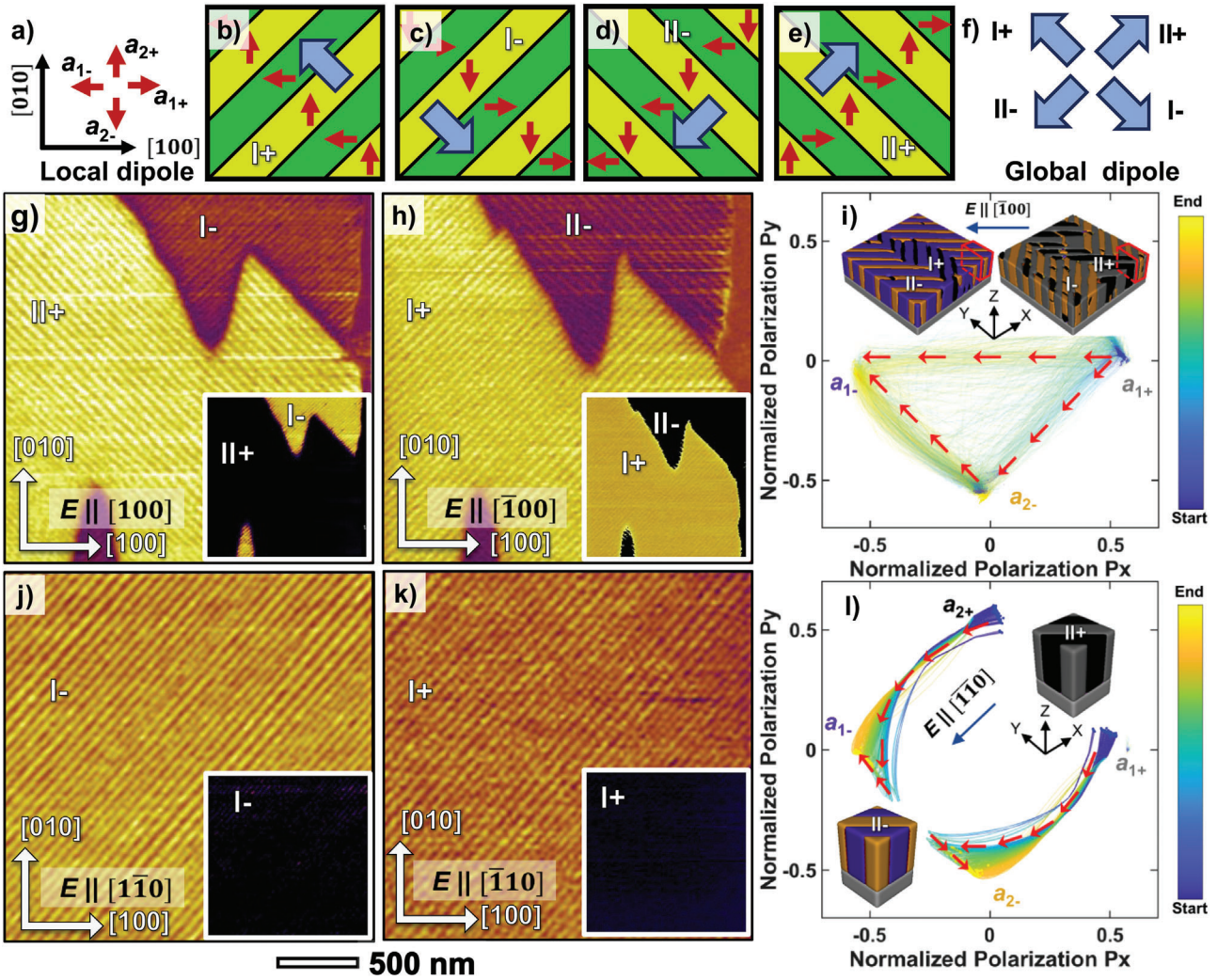

Figure 2. a) Different local domains based on the in-plane directions. Different superdomain types based on the global polarization direction. b) type I+, c) type I-, d) type II- and e) type II+. f) Representation of different global dipole directions based on superdomain types. g) L-PFM scan for a 0° device after applying *E* along the [100] showing type-I- and -II+ superdomains. Inset showing the corresponding phase of the superdomains. h) Same area is then analyzed after applying *E* along the [$\bar{1}$00] showing type-I+ and -II- superdomains. i) Switching pathway analyzed for a 0° device after application of *E* along the [$\bar{1}$00] on a type-I- superdomain variant subsection (shown in red color box) showing stepwise 90° switching and 180° switching pathway. j) L-PFM scan for a 45° device after applying *E* along the [1$\bar{1}$0] showing the resulting type-I- superdomain. Inset showing the corresponding phase of the superdomains. k) The same area is then analyzed after applying *E* along the [$\bar{1}$10] showing the resulting type-I+ superdomain. l) Switching pathway analyzed for a 45° device after applying *E* along the [$\bar{1}\bar{1}$0] on a type-II+ superdomain showing a 90° switching pathway to convert it into type-II- superdomain.

additional noteworthy observation is that the domain periodicity increases upon increasing the strontium content. Observation of large, single-variant regions would cause large local compressive or tensile strains. Domain formation like that seen here is an effective mechanism (that does not require the formation of interfacial misfit dislocations) to alleviate the formation of such high-strain regions by averaging the strain values in both in-plane directions (Figure S6a–c, Supporting Information). As the overall lattice parameters and tetragonality of the $Pb_{1-x}Sr_xTiO_3$ unit cell decrease with increasing strontium content, the lattice mismatch with the substrate consequently reduces (Figure S6d, Supporting Information). Therefore, a frequent requirement for forming such in-plane domain variants in both directions to avoid excessive local strain areas decreases, leading to the individual domain stripe size increment and overall periodicity. This provides an effective tool to tune domain periodicity other than thickness.[31]

Moving on from a static understanding of the as-grown domain structures, we can use L-PFM to probe the evolution of (and pathway for) switching in these in-plane polarized films. Here, a domain naming scheme is defined such that if the polarization is along the in-plane [100], [$\bar{1}$00], [010], and [0$\bar{1}$0] those domains are referred to as a_{1+}, a_{1-}, a_{2+}, and a_{2-} domains, respectively (**Figure 2**a). Assemblies of these small-scale a_1 and a_2 nanodomains can be further arranged in four types of "superdomains" which are related by 90° rotations (Figure 2b–e). These superdomains are further categorized as type I or II for those

with domain walls running along the [110] or [$\bar{1}$10], respectively. Additional + or – suffixes are added to these superdomain type names based on the type of a_2 domains included in the superdomain. For example, if the superdomain contains a_{2+} domains it would be the + variant and if it contained a_{2-} domains it would be the – variant. The resultant global in-plane component of polarization (blue arrow, Figure 2a–d) can now be defined and can lie along the [$\bar{1}$10] (type I+, Figure 2b), [1$\bar{1}$0] (type I-, Figure 2c), [110] (type II-, Figure 2d), or [$\bar{1}\bar{1}$0] (type II+, Figure 2e). Like local dipoles, these superdomains can be represented as global dipoles (Figure 2f). To study the dependence of applied electric field (***E***) direction on switching characteristics of various superdomains involving different combinations of local dipoles, planar device structures were fabricated on the top surface of the films (Experimental Section) such that in-plane ***E*** can be applied along the [100], [$\bar{1}$00], [010], or [0$\bar{1}$0] (henceforth referred to as *0° devices*, Figure S7a,b, Supporting Information) and the [110], [$\bar{1}$10], [1$\bar{1}$0], or [$\bar{1}\bar{1}$0] (henceforth referred to as *45° devices*, Figure S7c,d, Supporting Information).

E applied along the [100] results in the stabilization of two superdomain variants (type I- and II+, Figure 2g). Stabilization of these two superdomain variants, out of the four initial variants, is based on energy minimization by alignment of the resultant global polarization direction of the superdomains with the applied ***E***.[31,33] Upon applying the ***E*** along the [$\bar{1}$00] on the same structure (Figure 2g), the domains show characteristic switching wherein the superdomain boundaries remain essentially intact without any significant motion (Figure 2h), but the superdomains themselves show characteristic switching from type II+ to I+ and I- to II- via local a_1 and a_2 domain level switching. This superdomain switching is further explored by conducting additional large-area L-PFM scans and scans in other perpendicular direction (Figures S8, S9, Supporting Information).

To further understand the nature of switching, phase-field simulations (Experimental Section) were completed to map the switching pathways (Figure 2i) among multiple potential available routes (Figure S10, Supporting Information). The domain structure with two superdomain variants (here, type II+ and I-), was obtained by applying an electric field ***E*** along the [100], is used as a reference state (inset, Figure 2i). Upon reverse poling by applying ***E*** along the [$\bar{1}$00], the superdomains switch from type II+ to I+ and I- to II- via a nucleation-and-growth-like mechanism (Figure 2i; Figure S11, Supporting Information). To capture the local switching mechanism in response to the applied electric field ***E*** along the [$\bar{1}$00], we focus on the polarization evolution in a small subsection of one of these superdomains (within the simulation cell, marked by the red volume within the type-I- superdomain, Figure 2i), comprising two tetragonal domain variants – namely a_{1+} and a_{2-}. The phase-field simulations offer further insights into the switching pathways by providing the path each simulation cell takes (individual lines show the individual cell switching pathways and the red arrows show the overall, dominant pathways; Figure 2i). There are two dominant pathways, the first is a one-step process, where a single 90° switching event causes a_{1+} domains to become a_{2-} domains or a_{2-} domains to become a_{1-} domains. The second pathway is a two-step process in which the a_{1+} domains first switch to a_{2-} domains and then to a_{1-} domains. A small portion of a_{1+} domains also undergo a single 180° switching step to become a_{1-} domains and some a_{2-} domains do not undergo any switching. Thus, during this collective switching process, each unit-cell polarization responds to the applied ***E*** via one of the various switching pathways discussed above before moving to the final, elastically more compatible switched state within the superdomain boundary.

On the other hand, applying ***E*** along the [1$\bar{1}$0] leads to the stabilization of only type I-superdomains (Figure 2j). This selection is again based on energy minimization of the global polarization direction of the superdomain variant with applied ***E***.[31,33] Applying the ***E*** along the [$\bar{1}$10] on the same structure after initial poling, the superdomain shows no visible signs of domain pattern changes in L-PFM amplitude (Figure 2k). In reality, this superdomain variant rearranges itself via local single 90° switching events at the individual a_1 and a_2 domain level from a type-I- to a type-I+ superdomain. As was done for the 0° devices, additional large-area scans were carried out (Figures S12, S13, Supporting Information) and show that ordering within this single superdomain variant can occur over a considerable size (limited by the device size; Figure S14, Supporting Information).

As was done previously, further understanding of the nature of switching was gained via phase-field simulations for the 45° devices (Figure 2l; Figure S15, Supporting Information). Applying ***E*** along the [110] energetically favors two tetragonal domain variants (a_{1+} and a_{2+}) resulting in a single superdomain variant (type II+, Figure 2l). Upon reverse poling by applying ***E*** along the [$\bar{1}\bar{1}$0], the polarization in the two tetragonal domains will attempt to equally align with the electric field, creating an equal driving force for switching. This balance of driving forces eliminates the driving force for any domain-wall motion, leading to uniform switching along with maintenance of the local domain order in the in-plane direction (Figure S16, Supporting Information). Finally, this equal driving force creates two thermodynamically degenerate states (a_{1-} and a_{2-}), stabilizing a single superdomain variant (type II-, Figure 2l). The phase-field simulations provide further insight into the actual switching pathways (Figure 2l) and one can plot the path each simulation cell takes during the 45° device switching, where a single 90° switching step causes a_{1+} domains to become a_{2-} domains and a_{2+} domains to become a_{1-} domains. This notably changes the orientation of the electrostrictive strain (i.e., the polarization-induced or coupled strain) direction of the domains by 90°. During this collective switching process, each unit-cell polarization responds to the applied ***E*** by first rotating toward the same direction (i.e., parallel to [$\bar{1}\bar{1}$0]) before reaching the final, elastically more compatible switched state (individual lines show the individual cell switching pathways and the red arrows show the overall, dominant pathways, Figure 2l). Such robust control of in-plane domains and superdomains, guided by phase-field simulations, offers a promising perspective to design devices based on these in-plane domain structures.

To do just that, we focus on the 45° devices, which produce large-scale, single-superdomain-variant ordering upon poling. In turn, in-plane ferroelectric hysteresis loops (**Figure 3**a) were measured for 50-nm-thick $Pb_{1-x}Sr_xTiO_3$ (x = 0.4, 0.6, and 0.8) films at 1 kHz (Experimental Section). As-measured hysteresis loops include a background dielectric contribution which makes them

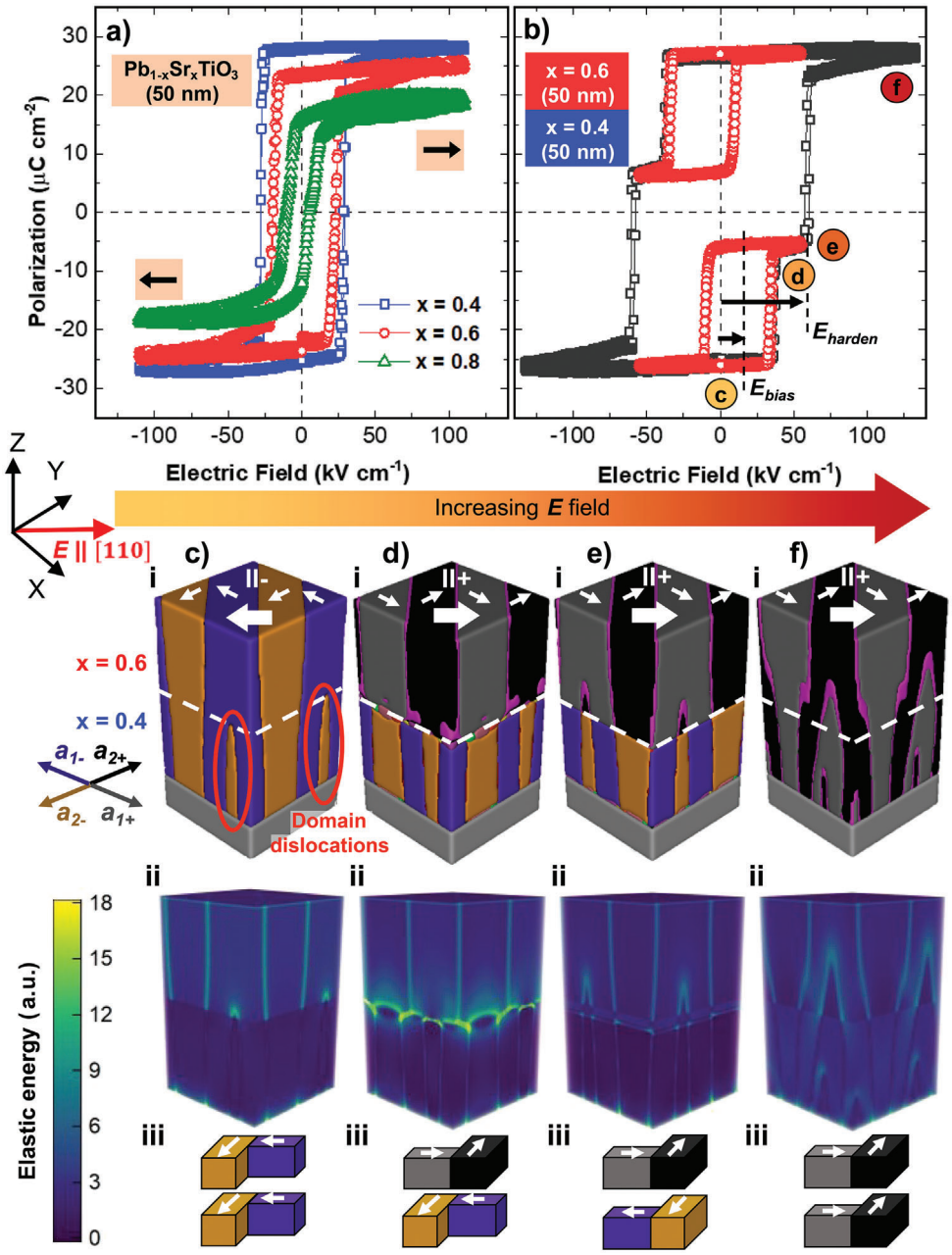

Figure 3. a) Polarization-electric field hysteresis loops measured at 1 kHz frequency for a 50-nm-thick $Pb_{0.2}Sr_{0.8}TiO_3$ (green), $Pb_{0.4}Sr_{0.6}TiO_3$ (red), and $Pb_{0.6}Sr_{0.4}TiO_3$ (blue) heterostructures. b) Bilayer of 50-nm-thick $Pb_{0.4}Sr_{0.6}TiO_3$ on top of 50-nm-thick $Pb_{0.6}Sr_{0.4}TiO_3$ exhibiting ferroelectric bias and coercivity hardening behavior with minor (red) and major (black) loops, respectively. Switching steps are further analyzed using phase-field simulations starting with c) the initial state, d) after the first switching event of the top $x = 0.6$ layer (The magenta regions at the domain wall between the a_{1+} and a_{2+} domains have polarization pointing along the [110]), e) after domain reshuffling in the bottom $x = 0.4$ layer, and f) after complete bilayer switching. For panels c–f), images i) show the equilibrium domain structure of the bilayer system, ii) show the corresponding elastic-energy distribution, and iii) show a simplified version of the domain arrangement at the interface at each switching step.

appear tilted; this has been subtracted for clarity (Figure S17, Supporting Information, Experimental Section). As previously observed for related systems in the out-of-plane direction,[35,39] both coercive field and remanent polarization decrease as a function of increasing strontium content. Hereafter, we transition to explore bilayer structures beginning with a 50-nm-thick $x = 0.6$ layer on top of a 50-nm-thick $x = 0.4$ layer. Under small $\boldsymbol{E}$ it is observed that only the top $x = 0.6$ film switches (Figure 3b) as was determined by the switched polarization value ($\Delta P = 22$ μC cm^{-2}) for the first switching event. The bottom $x = 0.4$ film switches only once the electric field exceeds ≈60 kV cm^{-1}, resulting in a complete switching of the bilayer system. The result is a two-step switching process that repeats itself under reverse poling (producing four distinct polarization states). To distinguish the

two switching events, the first switching event is referred to as the "minor loop" (and corresponds to the switching of the top $x = 0.6$ layer; Figure S18, Supporting Information, Experimental Section) and the second, larger switching event (corresponding to the complete switching of the bilayer system) is referred to as the "major loop". Both minor loops (one in the first half and the other in the second half of the bipolar waveform) are highlighted to aid the reader (red loops inside the major loop which is shown in black; Figure 3b). The minor loops are considerably shifted (for the bottom right side, by a bias field $\boldsymbol{E}_{bias}$= 14 kV cm^{-1}); a behavior analogous to exchange bias.

To better understand this effect, we need to consider two coupling phenomena that emerge when the ferroelectric films with in-plane polarization are placed in direct contact. The first is dipolar coupling which emerges from the electrostatic interaction of the polarization in the two layers and tends to align the polarization of the neighboring layers. The second is lattice coupling, which emerges from an elastic-energy interaction and works to form a domain of a similar type across the interface (i.e., it works to maintain domain continuity across the interface between the two layers). Such domain continuity effectively lowers the strain (elastic) energy cost of having the interface. As discussed earlier, the strontium content of a given layer (and assuming a constant substrate) can be used to engineer the domain periodicity. The lattice coupling, in turn, works to evolve both layers toward a similar strain state which requires similar domain orientation and periodicity in both layers of the bilayer. The phase-field simulations provide a detailed look at the equilibrium domain structure of the bilayer heterostructure at each switching step (Figure 3c–f, i) and the corresponding elastic-energy distribution for the bilayer throughout the switching process (Figure 3c–f, ii). Simplified domain-stacking schematics are also provided to help illustrate the cross-interface domain continuity of the bilayers (Figure 3c–f, iii). Using these three representations, we can explore the evolution of the bilayer systems under the applied field.

The initial state of the bilayer is a type-II- superdomain (Figure 3c, i) wherein individual a_{1-} and a_{2-} domains of the top $x = 0.6$ layer are aligned with the a_{1-} and a_{2-} domains of the bottom $x = 0.4$ layer. It is also found that the two layers have nearly matched domain periodicity, but that there are some additional small, needle-shaped domains in the bottom $x = 0.4$ layer which has intrinsically smaller domain periodicity; accommodated by dislocation-like domains or so-called "domain dislocations". This "matched" periodicity is also captured experimentally, where the common periodicity of λ_{RSM} = 56 nm (Figure S19c, Supporting Information) was observed for the bilayer structure. This periodicity is marginally higher than the intrinsic periodicity of the bottom $x = 0.4$ layer and the aforementioned "domain dislocations" form as the system tries to bridge between the elastic energy state of the two layers. Examining the elastic-energy density for the initial state (Figure 3c, ii), however, reveals that while the system has found a tentative equilibrium, there is some stored elastic energy in the system, especially in the top $x = 0.6$ layer and near the interface wherein the "domain dislocations" touch the interface. All told, however, the initial state of the system sees the same kind of domains aligning across the interface (Figure 3c, iii), albeit with some elastic frustration from intrinsic domain periodicity differences.

As the $\boldsymbol{E}$ is turned on and the system starts to evolve, the top $x = 0.6$ layer, which has a lower coercive field, switches first (Figure 3d, i). The increasing $\boldsymbol{E}$ along the [110] results in the rotation of local polarization by 90° (i.e., a_{1-} (purple) and a_{2-} (dark orange) to a_{2+} (black) and a_{1+} (gray), respectively; Figure 3d, i), and the corresponding transformation of the electrostrictive strain related to the initial type-II- superdomain in the top $x = 0.6$ layer to a type-II+ superdomain. As the global dipole associated with the type-II+ superdomain aligns perfectly with applied $\boldsymbol{E}$ with these single 90° switching steps, it does not need to follow other switching routes (e.g., double 90° switching steps or a single 180° switching step; Figure S15, Supporting Information) to achieve the same required superdomain state; a mechanism explained previously for single-layer 45° devices. This 90° rotation of the electrostrictive strain of the top layer, however, creates elastically incompatible perpendicular electrostrictive strain at the interface since the bottom layer does not rotate yet. As the a_{1-} (a_{2-}) domains of the top $x = 0.6$ layer switch to a_{2+} (a_{1+}), the bilayer finds a new equilibrium wherein those domains interface with a_{1-} (a_{2-}) domains in the bottom $x = 0.4$ layer. This elastic incompatibility is clearly seen in the elastic-energy density (Figure 3d, ii), wherein there is high elastic energy stored at the interface. This also creates additional domain walls at each of the a_1 and a_2 stripes across the interface and a 90° alignment between polarization states across the interface as can be schematically seen from the overall domain picture (Figure 3d, iii). The result, therefore, is that the switching should be anisotropic and energetically expensive due to the formation of such substantial discontinuity in spontaneous strain and polarization across the interface during this first switching event, leading to an exchange-bias-like shift in the form of a higher magnitude of the positive-coercive field than that of the negative-coercive field (Figure 3b). Similar behavior was observed in the reverse switching direction of the major loop (Figure 3b) in the form of a higher magnitude of negative-coercive field than that of the positive one. This "ferroelectric bias" is thus tunable on both sides via an electric field compared to previously reported defect-based ferroelectric bias, where field cooling was essential to change the bias direction.[18]

From the ferroelectric hysteresis loops (Figure 3b) it is also evident that the coercive field of the bottom $x = 0.4$ layer is enhanced (hardened) to $\boldsymbol{E}_{harden}$= 60 kV cm^{-1} as compared to its value in isolation ($\boldsymbol{E}_c$ = 30 kV cm^{-1}). This can be understood by taking into consideration the strain mismatch at the interface (Figure 3d, ii). This strain mismatch drives the reorganizing of the domain structure in the bottom $x = 0.4$ layer where the a_{1-} (purple) and a_{2-} (dark orange) domains redistribute their fraction (periodicity) and partially switch to a_{2-} (dark orange) and a_{1-} (purple), respectively, without an overall ferroelectric switch of the entire layer (Figure 3e, i). This rearrangement of the domain structure in the bottom $x = 0.4$ layer works to make the system more elastically compatible and effectively lowers the elastic-energy density at the interface (Figure 3e, ii). Thus, the overall domain structure of the bilayer adjusts to prefer 180° alignment of polarization across the interface thereby placing a_{1-} and a_{1+} and a_{2-} and a_{2+} domains in contact (Figure 3e, iii). This domain "reshuffling" does, however, lead to an additional energy penalty resulting in the form of "coercivity hardening" before ferroelectric switching for the bottom $x = 0.4$ layer (Figure 3b). Ferroelectric switching begins from

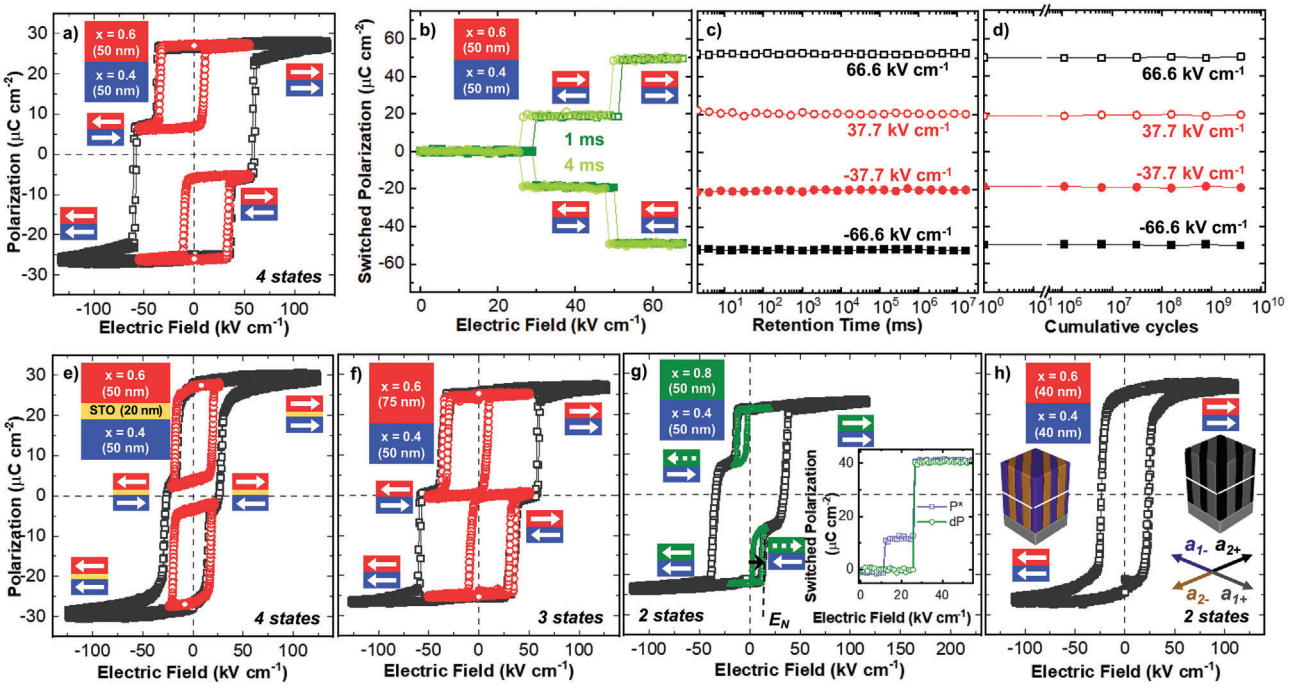

Figure 4. Polarization-electric field hysteresis loops measured at 1 kHz frequency for a) bilayer of 50 nm-thick $Pb_{0.4}Sr_{0.6}TiO_3$ on top of 50-nm-thick $Pb_{0.6}Sr_{0.4}TiO_3$ exhibiting four states. b) The PUND studies reveal the pathway to the different polarization states at a constant pulse width of 1 and 4 ms as a function of different pulse voltages. c) The long-term retention and stability of the multiple polarization states. d) Stability of the multiple polarization states after long fatigue cycles. e) Bilayer of 50-nm-thick $Pb_{0.4}Sr_{0.6}TiO_3$ on top of 50-nm-thick $Pb_{0.6}Sr_{0.4}TiO_3$ separated by a 20-nm-thick $SrTiO_3$ spacer layer exhibiting lattice decoupling phenomenon. f) Polarization-electric field hysteresis loops for a bilayer of 75-nm-thick $Pb_{0.4}Sr_{0.6}TiO_3$ on top of 50-nm-thick $Pb_{0.6}Sr_{0.4}TiO_3$ exhibiting three distinct states. g) Bilayer of 50-nm-thick $Pb_{0.2}Sr_{0.8}TiO_3$ on top of 50-nm-thick $Pb_{0.6}Sr_{0.4}TiO_3$ exhibiting exchange-spring-like behavior. h) Bilayer of 40-nm-thick $Pb_{0.4}Sr_{0.6}TiO_3$ on top of 40-nm-thick $Pb_{0.6}Sr_{0.4}TiO_3$ exhibiting two states with coercivity softening of the hard layer.

the substrate side after the completion of the domain reshuffling process in the bottom $x = 0.4$ layer (Figure 3e, ii). Finally, increasing $\boldsymbol{E}$ further results in the bottom $x = 0.4$ layer switching completely (Figure 3f, i) without generating a high elastic-energy density at the interface (Figure 3f, ii). The final configuration (as one would expect) mirrors the initial state in that the same kind of domain types are present across the interface (Figure 3f, iii). Importantly, after completing the bilayer switching process, domain dislocations can be seen to remain in the bottom $x = 0.4$ layer (Figure 3f, i) and their influence can be seen in the reverse switching direction of the hysteresis loop (Figure 3b) with similar biasing and coercivity hardening effects. Some small extensions of existing domain dislocations for the bottom $x = 0.4$ layer into the top $x = 0.6$ layer lead to a (slightly) different elastic energy distribution for the final state (Figure 3f, ii) as compared to the initial state (Figure 3c, ii). The phase-field simulations not only provide an ability to watch how switching evolves in these multilayer structures, but can also be used to extract simulated versions of the ferroelectric polarization-electric field hysteresis loops which aptly recreate the two-step switching process observed experimentally (Figure S20, Supporting Information). All told such a bilayer system with strong interlayer coupling gives rise to a complex, interdependent domain-switching process that allows one to produce effects not commonly seen in single layers alone and, in turn, opens avenues to explore device designs beyond traditional purely substrate-controlled domain engineering pathways.

With this in mind, we extend the analysis of the switching behavior of the same $x = 0.6$ / $x = 0.4$ bilayer system. First, we bring forward (for reference) the overall ferroelectric polarization-electric field hysteresis loop shown previously which revealed that the intermediate polarization states produced by the minor loop (i.e., switching the top $x = 0.6$ layer) are stable (red loops crossing at $\boldsymbol{E} = 0$ kV cm^{-1} with non-zero remanent polarization, **Figure 4**a). Further assessment of this data reveals that the first switching event effectively creates a stable, remanent polarization value of +/−6 μC cm^{-2} and complete switching of the bilayer results in a stable, remanent polarization value of +/−26 μC cm^{-2}. As the two states have been observed in both the forward and reverse switching directions, the system exhibits four different states. Additional pulsed-switching studies (PUND, Experimental Section) were used to further interrogate the nature of these four distinct polarization states (Figure 4b; Figure S21, Supporting Information). It was found that one can independently access all four states – meaning that one can go from one state to any other state as desired. Furthermore, all four states in the bilayer heterostructures were found to be highly stable and showed minimal change in polarization with time in retention testing (Figure 4c; Figure S22, Supporting Information, Experimental Section). While the retention testing showed stability out to over five hours, other tests have shown the states to be stable for more than 200 days and, to the best of knowledge, they are stable well beyond this. Likewise, the endurance of each polarization state was also explored using a fatigue-pulse sequence (Figure 4d;

Figure S23, Supporting Information, Experimental Section), and it was found that each state could be repeatedly accessed and was easily distinguishable even after $>10^9$ write cycles. These results indicate several essential features required for robust multistate operation.

To bring home the analogy with magnetic systems and confirm that these effects truly arise from cross-interface coupling, a 20-nm-thick $SrTiO_3$ dielectric buffer layer was added in the middle of the same heterostructure such that it is now an $x = 0.6$ / $SrTiO_3$ / $x = 0.4$ trilayer system. With the $SrTiO_3$ layer present, the minor loop showed minimal horizontal shift (≈1.4 kV cm^{-1}; red loops, Figure 4e). Additionally, the minor loops showed stable remnant polarization after the first switching event, demonstrating effective decoupling. This decoupling is also reflected in structural characterization, where each layer's domain periodicity returned to close to its original periodicity for the 50-nm-thick individual films (Figure S24, Supporting Information). The thickness of the $SrTiO_3$ spacer layer required to decouple the two adjoining ferroelectric layers is set by how the electric and elastic fields depend upon the polarization value of each ferroelectric layer, the magnitude of the ferroelectric proximity induced dipole–dipole interaction strength,[40] and the polarization due to substrate-induced epitaxial strain.[41] This is consistent with what has been previously observed in the order-disorder transition in superlattices exhibiting polar vortices[41] and in ferroelectric proximity effects in ferroelectric bilayers.[40] In essence, the electric and elastic fields in the $SrTiO_3$ layer decay with increasing distance, a distance that scales with the polarization of the adjoining ferroelectric layers and with the strain.

Having established the robust nature of the multistate polarization and cross-interface coupling produced in these bilayer structures, we proceeded to use our knowledge of the individual layers to further manipulate the nature of multistate switching and to demonstrate the flexibility of such heterostructures to produce novel functions. First, we explored the use of layer thickness to control the polarization value of the distinct intermediate states. For example, in a similar bilayer heterostructure but with a 75-nm-thick top $x = 0.6$ layer and a 50-nm-thick bottom $x = 0.4$ layer, it is possible to produce a minor loop in both the positive and negative half of the switching cycle that has a stable intermediate polarization value of 0 μC cm^{-2} (red loop, Figure 4f). Thus, here it is possible to make a three-state system (as opposed to the four-states shown before). With this as an example, the flexibility of these heterostructures to produce on-demand polarization states is demonstrated. Furthermore, the $\boldsymbol{E}_{bias}$= 13.8 kV cm^{-1} for this bilayer is essentially the same as that observed for that from the 50-nm-thick $x = 0.6$ layer on top of a 50-nm-thick $x = 0.4$ layer, suggesting that varying the thickness of the soft layer (here, the $x = 0.6$ layer) has little to no influence on the magnitude of $\boldsymbol{E}_{bias}$. In turn, we also explored the use of changing the chemistry of the layers to demonstrate further control. Again, in a similar bilayer heterostructure but with a 50-nm-thick top $x = 0.8$ layer and 50-nm-thick bottom $x = 0.4$ layer, it was found that the switching of the top $x = 0.8$ layer was not stable, as captured by the minor loop displaying no remanence (green loops, Figure 4g). Here, $\boldsymbol{E}_{bias}$= 7 kV cm^{-1} was observed and suggests that lowering the magnitude of the polarization of the soft ferroelectric layer (here, the $x = 0.8$ layer), which arises from the further introduction of strontium and a lowering of the tetragonality, leads to lower anisotropy during the first 90° switching event and, thus, a lower $\boldsymbol{E}_{bias}$ value. In other words, the lower the switched polarization value of the soft layer, the lower the $\boldsymbol{E}_{bias}$ value. Pulsed-switching studies for the positive side (inset, Figure 4g) also showed no stable remanence (dP) after the first switching event (P^*), demonstrating that the switched top $x = 0.8$ layer returns to its initial configuration, akin to a spring. After the second switching event (i.e., of the bottom $x = 0.4$ layer), both layers showed stable switching without any backswitching as captured by the hysteresis loop and also with the pulsed-switching studies. Similar behavior was observed on the negative side (Figure S25, Supporting Information). This behavior is similar to the ESM concept introduced before, wherein the appropriate couples of hard and soft ferromagnets exhibit the high anisotropy and coercive fields of the hard magnet, with an enhanced magnetic moment coming from the soft magnet. In ESMs, the coupling appears below a certain critical thickness of the soft layer, leading to a simultaneous magnetization reversal process. When this critical value is exceeded, a two-step feature appears in the hysteresis loop of the system.[42] A similar kind of coupling is observed here, but in this case, it is between the lattice and, in turn, polarization dipoles in two different in-plane polarized ferroelectric layers. The hard and soft ferroelectric layers are again defined based on the coercive field of each ferroelectric. The soft, in-plane ferroelectric layer (i.e., the top $x = 0.8$ layer) is pinned firmly to the hard layer (i.e., the bottom $x = 0.4$ layer) at the interface. The top $x = 0.8$ layer starts switching only when the applied $\boldsymbol{E}$ exceeds the electric field denoted as the bending or nucleation field ($\boldsymbol{E}_N$), which is the same as of positive coercivity field here. Upon reducing the applied $\boldsymbol{E}$ before the second switching event (i.e., that of the bottom $x = 0.4$ layer), backswitching of the soft, top $x = 0.8$ layer happens in a "springy" nature which returns it to its original state as captured by the minor loops.

In ESMs, there is also a critical thickness below which the soft magnet is rigidly coupled to the hard one, and the two phases reverse at the same nucleation field resulting in a rectangular hysteresis.[42] Similar thickness-dependence is observed in the ferroelectric bilayers. For example, when a bilayer heterostructure of the form of a 40-nm-thick top $x = 0.6$ layer and a 40-nm-thick bottom $x = 0.4$ layer is probed, it is observed that the entire system switches, in a single event, at $\boldsymbol{E}$ = 23 kV cm^{-1}; which is lower than the coercive field of the bottom $x = 0.4$ layer alone ($\boldsymbol{E}_c$ = 30 kV cm^{-1}) but close to that of top $x = 0.6$ layer ($\boldsymbol{E}_c$ = 22 kV cm^{-1}). In essence, the bilayer can be controlled to give rise to "coercivity softening". As the individual layers become thinner, the domain periodicity difference between the two layers reduces[31] and the average distance from the bilayer interface becomes smaller, thus increasing the effective coupling between the films. This causes the individual a_1 and a_2 domain stripes in each layer (more) perfectly match across the interface without exhibiting any "domain dislocations" in the bottom $x = 0.4$ layer (Figure 4h; Figure S26a, Supporting Information). The periodicity matching phenomenon is also captured experimentally, where the common periodicity of λ_{RSM} = 50 nm (Figure S27, Supporting Information) was observed for the bilayer structure. This, furthermore, effectively changes the bilayer switching mechanism. Simulations show that no domain reshuffling occurs in the bottom layer in the absence of domain dislo-

cations, eliminating the kinetic pathway for multistate switching. This also creates a high elastic energy interface cost between the top, switched, soft layer and the bottom, unswitched, hard layer acting as an additional driving force to switch, thus inducing the hard layer to switch at a lower ***E*** value than the coercive field of that its isolated version of the hard layer (Figure S28, Supporting Information). This behavior is, again, similar to that observed in ESMs where the decrease of coercivity of the hard ferromagnet is explained by the propagation of the domain wall formed in the soft ferromagnet compressing against the interface and then propagating further, reducing the coercive field of the hard phase.[42–44] Thus, the geometrical arrangement of domains and polarization in the in-plane ferroelectrics offers access to a wide design space and access to phenomena largely unexplored and inaccessible in prototypical ferroelectric heterostructures made up of out-of-plane polarized domains. These findings signify that the in-plane bilayer ferroelectrics can also be engineered in ways similar to their magnetic cousins and can exhibit effects analogous to exchange-bias and exchange-spring effects via lattice and polarization coupling.

3. Conclusion

All told, by combining epitaxial thin-film growth, detailed structural characterization, ferroelectric switching studies, and phase-field simulations, we have systematically investigated the interlayer interactions between in-plane polarized ferroelectric layers in bilayer $Pb_{1-x}Sr_xTiO_3$ heterostructures. The combination of strain, chemistry, thickness, and device geometry provides a fine level of control of the domain patterns and their arrangement. In turn, these structures have been analyzed in the bilayer configuration for their interlayer coupling-induced exchange-bias-like phenomenon, an idea adapted from the exchange interactions in magnetism. This electric analog of exchange bias in the ferroelectric system can be additionally tuned via an electric field, providing added control of the system, which is then used to realize multistate functionality. Further control via strontium content and thickness selection has shown springy switching nature and coercivity reduction in the bilayer system, respectively, which is analogous to exchange spring in magnetism. Thus, this bilayer system provides a rich playground for tuning interlayer coupling across the system.

4. Experimental Section

Pulsed-Laser Deposition of Thin-Film Heterostructures: All films were grown using pulsed-laser deposition in an on-axis geometry with a target-to-substrate distance of 60 mm, using a KrF excimer laser (248 nm, LPX 300, Coherent). All films were grown from $Pb_{1.2}TiO_3$ ceramic (K. J. Lesker) and $SrTiO_3$ single-crystal targets. The 20% excess lead in the $Pb_{1.2}TiO_3$ target was found to be vital to compensate for the lead loss during the $PbTiO_3$ thin film growth. The growth rate was established for individual, single-layer $PbTiO_3$ and $SrTiO_3$ thin films grown on $DyScO_3$ (110) substrates (CrysTec GmbH) using X-ray reflectivity. The composition of the $Pb_{1-x}Sr_xTiO_3$ thin-film heterostructures was varied across $0.4 \leq x \leq 0.8$ using a sub-unit-cell-level mixing method from the $Pb_{1.2}TiO_3$ ceramic (K. J. Lesker) and $SrTiO_3$ single-crystal target via a programmable target rotator (Neocera, LLC) that was synced in real-time with the excimer laser. For example, here, it took 60 pulses to grew a unit cell of $PbTiO_3$ and 50 pulses to grew a unit cell of $SrTiO_3$. Therefore, a $Pb_{0.6}Sr_{0.4}TiO_3$ film could be achieved by growing a sequence of 18 pulses of $PbTiO_3$, 10 pulses of $SrTiO_3$, 18 pulses of $PbTiO_3$ and 10 pulses of $SrTiO_3$ (for a total of 56 pulses; 36 from $PbTiO_3$ and 20 from $SrTiO_3$ making the right composition) overall. This approach was used in numerous prior works.[19,20,45–47] The growth of the $Pb_{1-x}Sr_xTiO_3$ thin films ($0.4 \leq x \leq 0.8$) was completed on $DyScO_3$ (110) single-crystal substrates at a heater temperature of 640 °C, a dynamic oxygen pressure of 10 mTorr, a laser fluence of 1.8 J cm^{-2}, and the laser repetition rate was 10 and 2 Hz for growth of $Pb_{1.2}TiO_3$ and $SrTiO_3$, respectively. Bilayer films of the specific compositional sequence were also grown using a similar method. Following growth, the films were cooled to room temperature at a static oxygen pressure of 700 Torr.

Determination of Crystal Structure via X-Ray Diffraction: The crystal structure of the $Pb_{1-x}Sr_xTiO_3$ films was determined using X-ray diffraction using a high-resolution X-ray diffractometer (Panalytical, X'Pert MRD) with fixed-incident-optics slits of 1/2° for θ–2θ and 1/32° for RSM studies, copper K_α radiation (1.54 Å), and a fixed receiving slit of 0.275 mm for a PIXcel3D-Medipix3 detector. θ–2θ line scans were performed to investigate the domain structures in the direction perpendicular to the plane of the $DyScO_3$ (110) substrates. In addition, X-ray diffraction RSM studies were performed about the 220_O-, 332_O-, and 240_O-diffraction conditions of the $DyScO_3$ (110) substrate to determine the lateral domain periodicity of in-plane domain variants.

Topography and Domain Structure Characterization: A study of the topography of the $Pb_{1-x}Sr_xTiO_3$ thin films was carried out using an atomic force microscope (AFM) (MFP-3D, Asylum Research). All topography measurements were carried out using silicon AFM probe tips (Tap300Al-G, BudgetSensor) with a force constant of 40 Nm^{-1} at a resonance frequency of ≈300 kHz using the AC Air Topography mode (non-contact tapping mode). The PFM studies were carried out using the same MFP-3D AFM (Asylum Research) system using Ir/Pt-coated conductive tips (Nanosensor, PPP-NCLPt, force constant ≈48 Nm^{-1}). Dual AC Resonance Tracking Piezo Force Microscopy (DART-PFM) mode was used to perform in-plane (lateral) PFM at a central frequency of ≈670 kHz and out-of-plane PFM at a central frequency of ≈320 kHz to image the domain structures.

Phase-Field Simulations: The phase-field models for ferroelectrics were used to simulate the temporal evolution of polarization in single-layer and bilayer $Pb_{1-x}Sr_xTiO_3$ thin films. In the phase-field models, the time evolution of the polarization field was described by the time-dependent Ginzburg–Landau equation:

$$\frac{\partial P_i(\mathbf{r}, t)}{\partial t} = -L\frac{\delta F}{\delta P_i(\mathbf{r}, t)} \tag{1}$$

where P_i represents the spontaneous polarization (measured in C m^{-2}), ***r*** represents the position in space, t is time, and L is the kinetic coefficient relating to the domain-wall motion. The total free energy functional (F) contained the following energy-density terms.

$$F = \int_V \left(f_{Landau} + f_{Elastic} + f_{Electric} + f_{Gradient}\right) d^3\mathbf{r} \tag{2}$$

Following the Landau theory of phase transformations, f_{Landau} is the Landau free energy of the $Pb_{1-x}Sr_xTiO_3$ (PSTO) system was described by a sixth-order polynomial expansion about the polarization order parameter:

$$\begin{aligned} f_{Landau}\ (P_i) = {} & \alpha_1\left(P_1^2 + P_2^2 + P_3^2\right) + \alpha_{11}\left(P_1^4 + P_2^4 + P_3^4\right) \\ & + \alpha_{12}\left(P_1^2P_2^2 + P_1^1P_3^2 + P_2^2P_3^2\right) + \alpha_{111}\left(P_1^6 + P_2^6 + P_3^6\right) \\ & + \alpha_{112}\left(P_1^4\left(P_2^2 + P_3^2\right) + P_2^4\left(P_1^2 + P_3^2\right) + P_3^4\left(P_2^2 + P_1^2\right)\right) \\ & + \alpha_{123}P_1^2P_2^2P_3^2 \end{aligned} \tag{3}$$

where α_i, α_{ij}, and α_{ijk} are the dielectric stiffness coefficients measured under constant stress. For $Pb_{1-x}Sr_xTiO_3$, the coefficients were calculated as weighted averages of those for pure $PbTiO_3$[48] and $SrTiO_3$,[49] except for

α_1 where the linearly averaged dielectric stiffness was employed as previously used in the literature:[50]

$$\alpha_1 = 5.65 \times 10^5 \ (T - 716.5x_{Pb} + 237.5) \ / \ (0.81 + 0.69x_{Pb}) \quad (4)$$

where T is the temperature in °C and x_{Pb} denotes the mole fraction of lead in the solid solution $Pb_{1-x}Sr_xTiO_3$. The other dielectric stiffness coefficients are $\alpha_{11} = -7.3 \times 10^7 x_{Pb} + 1.04 \times 10^8(1 - x_{Pb})$, $\alpha_{12} = 7.5 \times 10^8 x_{Pb} + 7.46 \times 10^7(1 - x_{Pb})$, $\alpha_{111} = 2.6 \times 10^8 x_{Pb}$, $\alpha_{112} = 6.1 \times 10^8 x_{Pb}$, and $\alpha_{123} = -3.7 \times 10^9 x_{Pb}$.

The elastic energy density is expressed as,

$$f_{Elastic} = c_{ijkl} \left(\varepsilon_{ij} - \varepsilon^0_{ij}\right)\left(\varepsilon_{kl} - \varepsilon^0_{kl}\right) \quad (5)$$

$$\varepsilon^0_{ij} = Q_{ijkl} \ P_k P_l \quad (6)$$

where c_{ijkl} represents the elastic stiffness tensor, Q_{ijkl} is the electrostrictive tensor, ε_{ij} is the total strain, and ε^0_{ij} is the stress-free strain (or eigenstrain) which is related to the magnitude of the polarization. The elastic-energy coefficients are $Q_{11} = 0.089x_{Pb} + 0.0496(1 - x_{Pb})$, $Q_{12} = -0.026x_{Pb} - 0.0131(1 - x_{Pb})$, $Q_{44} = 0.0675x_{Pb} + 0.019(1 - x_{Pb})$, $S_{11} = 8.0 \times 10^{-12}$, $S_{12} = -2.5 \times 10^{-12}$, and $S_{44} = 9.0 \times 10^{-12}$.

The electrostatic-energy density is given by:

$$f_{Electric} = -\frac{1}{2}\kappa_0 \kappa^b_{ij} E_i E_j - E_i P_i \quad (7)$$

where $\kappa_0$is the vacuum permittivity and k^b_{ij} is the background dielectric constant which is chosen as 45 and to be isotropic. A uniform $\boldsymbol{E}$ was applied along the (110) ranging from −280 to 280 kV cm^{-1} for the single-layer- and bilayer-switching calculations. Further information on solving the elastic and electrostatic equilibrium equations could be found in the literature.[51]

The local gradient energy contribution can be defined as,

$$f_{Gradient} = \frac{1}{2} G_{ijkl} \frac{\partial P_i}{\partial x_j} \frac{\partial P_k}{\partial x_l} \quad (8)$$

where an isotropic gradient-energy tensor, G_{ijkl}, was assumed with renormalized values of $G_{11} = 0.60$, $G_{12} = -0.60$, and $G_{44} = 0.60$ in Voigt notation.

For the bilayer-switching simulations, a system size of $(64\Delta x_1 \times 64\Delta x_2 \times (h + 24)\Delta x_3)$ was used. Here, h represents the thickness of the film with $h\Delta x_3$ grid points as the ferroelectric film, there were $20\Delta x_3$ grid points as the substrate, the elastic constants were assumed to be the same as the film, and there were $4\Delta x_3$ grid points acted as a vacuum layer above the film. Periodic boundary conditions were applied for the in-plane lateral directions, whereas natural boundary conditions were applied to the film-vacuum and film-substrate interfaces. In all simulations $\Delta x_1 = \Delta x_2 = \Delta x_3 = 1$ nm. The bilayer structure was expressed by spatially varying the material properties (i.e., the Landau coefficients, elastic stiffness, etc.) using a sharp interface description. The interface between the film and substrate was assumed to be coherent. Therefore, the lattice mismatch strains between the $DyScO_3$ (110) (DSO) substrate and the PSTO films were calculated using the pseudocubic lattice constant for PSTO[52] (i.e., $a^{PC}_{PSTO} = (a^2_{PSTO} C_{PSTO})^{1/3}$) and the pseudocubic lattice parameters of DSO.[53] Since the lattices of the film and substrate were orthogonal, there was no in-plane shear misfit strain such that:

$$\varepsilon_{11} = \frac{a^{[100]}_{DSO} - a^{PC}_{PSTO}}{a^{[100]}_{DSO}}, \varepsilon_{22} = \frac{a^{[010]}_{DSO} - a^{PC}_{PSTO}}{a^{[010]}_{DSO}}, \varepsilon_{12} = \varepsilon_{21} = 0 \quad (9)$$

To initiate the simulation, random noise was applied to each spatial vector point, and the simulation was evolved to a steady-state condition. Next, the electric field was applied to simulate the switching behaviors with the electric field $\boldsymbol{E}$ changing by 4 V cm^{-1} for each time step. The phase-field calculations were completed using the μPro software. Visualization of the domain structures was completed using a homegrown application using the Visualization ToolKit.

In-Plane Device Fabrication: In-plane device structures were patterned via UV lithography using a Heidelberg MLA150 Maskless Aligner in the Berkeley Marvell NanoLab using AZ MiR 701 Photoresist. For these devices, the finger length was 120 µm and finger spacings of 2, 3, 4, and 5 µm were used. After patterning, a layer of ≈5 nm of titanium (which was used as an adhesion layer) and a layer of ≈80 nm of platinum was deposited at room temperature via DC magnetron sputtering at an argon pressure of 2 mTorr (base pressure of ≈10^{-8} Torr). The additional metal deposited outside the primary device structure was then lifted off via an approximately five-hour soak in 1-methyl-2-pyrrolidone (NMP) at 85 °C which was maintained using a hot plate (Thermo Scientific HP88854100 Cimarec+ Digital Hotplate).

Ferroelectric Hysteresis Loop Measurements: Polarization-electric field hysteresis loops were measured using a Precision Multiferroic Tester (Radiant Technologies, Inc.). The hysteresis loop measurements were performed at 1 kHz with a double bipolar waveform at an amplitude varying from 10 to 80 V, depending on the measurement requirements. To contact the sample electrodes, tungsten probe tips (model 7-B, The Micromanipulator Company) were used with a point radius of 0.5 µm. First, polarization-electric field hysteresis loops were captured for a given sample using in-plane platinum devices (Figure S17a, Supporting Information). Due to the device geometry, the hysteresis loops included a ferroelectric switching signal and a dielectric background signal. Linear fitting was done at both ends at the high-field region (positive and negative), where the signal predominantly came from the dielectric background (Figure S17a, Supporting Information). The equation of a single line was then calculated (Figure S17b, Supporting Information) by taking an average of the slope and linear intercept of previously assessed two linearly fitted lines at the high-field regions (positive and negative). This linear equation was then subtracted from the raw hysteresis loop data to get switched polarization-only data (Figure S17c, Supporting Information).

Ferroelectric Hysteresis Measurements for Minor Loops: To capture the minor loop associated with the first switching event on the positive side of the loop, first, a double bipolar waveform with voltage amplitude ($V_{full\text{-}loop}$) large enough to switch both layers in the bilayer system was applied as shown (Figure S18a, Supporting Information). This waveform captured all four states related to the entire switching cycle (Figure S18b, Supporting Information). The end state of this bipolar waveform was zero volts, which was approached explicitly from the negative voltage side. This waveform configuration led both layers of the bilayer system to be poled negatively as shown (bottom left, Figure S18b, Supporting Information). Next, to capture the minor loop switching event on the positive side of the hysteresis loop, a similar waveform, but this time just enough to switch the top layer ($V_{sub\text{-}loop}$) was applied in the bipolar waveform as shown (Figure S18c, Supporting Information). Again, this waveform should start from zero volts and rose to the voltage amplitude of $V_{sub\text{-}loop}$ in the positive direction in the first quadrant. This waveform would apply just enough voltage to switch the layer responsible for the first switching event of the bilayer from the fully negatively poled initial state (Figure S18d, Supporting Information). This minor loop was then normalized with the complete bilayer thickness, effectively halving the polarization value in this case (Figure S18e, Supporting Information). This minor loop could then be adjusted vertically to match the first switching event of the major loop captured initially (Figure S18f, Supporting Information).

Positive-Up-Negative-Down (PUND) Measurements: Pulsed-switching measurements were performed using the PUND pulse sequence on the in-plane device structures using a Precision Multiferroic Tester (Radiant Technologies, Inc.). PUND tests were used to study the multistate switching behavior of the bilayer heterostructures. A conventional PUND pulse sequence was used in these measurements (Figure S21, Supporting Information). Each measurement cycle was made up of five pulses comprising

one preset pulse and four reading pulses with specific voltages and widths. A large preset voltage was applied at the beginning of each cycle to pre-pole the in-plane domain architecture to the $-V$ direction; no measurement was performed for this pulse. The pulse width was kept constant ($t = 1$ and 4 ms in this work), while the pulse voltage was increased by 0.5 V for each consecutive cycle. The second pulse switched the in-plane domains to the $+V$ direction and measured the amount of switched polarization. The third pulse was an exact replica of the second pulse, which was used to read the non-remanent part of polarization along with the dielectric background, which dissipated during the delay time after the second pulse. The fourth and fifth pulses mirrored the second and third and switched the capacitor to the $-V$ direction and read both the switched and non-switched polarization, respectively. The delay time between all the pulses was set to $t = 100$ ms to let the in-plane domain structures backswitch (if required). These measurements produced $\pm P^*$, $\pm P^*_r$, $\pm \hat{P}$ and $\pm \hat{P}_r$ and $\Delta P = P^* - \hat{P}$, $\Delta P_r = P^*_r - \hat{P}_r$, $-\Delta P = -P^* - (-\hat{P})$ and $-\Delta P_r = -P^*_r - (-\hat{P}_r)$. Here, the asterisk (*) represents the total of remanent and non-remanent polarization components and r represents the remanent polarization component only. $+P^*$ ($-P^*$) was measured at the end of the second (fourth) pulse when the voltage was on, and $+P^*_r$ ($-P^*_r$) was measured after a certain amount of delay time (100 ms) when the voltage was off after the second (fourth) pulse. $+\hat{P}$ ($-\hat{P}$) was measured at the end of the third (fifth) pulse when the voltage was on, and $+\hat{P}_r$ ($-\hat{P}_r$) was measured after a certain amount of delay time (100 ms) when the voltage was off after the third (fifth) pulse. These four terms (ΔP, $-\Delta P$, ΔP_r, $-\Delta P_r$) defined here were four different calculations of the remanent polarization only and had produced very similar results.

Retention Measurements: The retention measurements were performed using a Precision Multiferroic Tester (Radiant Technologies, Inc.). Like the PUND measurements, a large preset voltage (here, −50 V applied for 1 ms) was applied at the beginning of each cycle to pre-pole the in-plane domain structures to a negative direction; no measurement was performed for this pulse (Figure S22, Supporting Information). Each polarization state was first accessed using an appropriate pulse width and voltage which were extracted from the previously shown PUND measurements. For example, 18 V and 1 ms for the partly switched intermediate state on the positive side of the hysteresis loop of the bilayer heterostructures of the form 50-nm-thick top $x = 0.6$ layer and 50-nm-thick bottom $x = 0.4$ layer, and 32 V and 1 ms for the completely switched state. The system was then held at zero voltage for a specific retention time. In this case, starting with a 2 ms retention time and then doubling for each successive cycle. After each writing cycle and the retention wait period, a reading pulse and non-switching pulse (−40 V and 1 ms) were subsequently applied to analyze the retention behavior of the switched polarization. A similar process was repeated on the negative side to get characteristics of the retention behavior on the negative side of the switched polarization.

Fatigue Measurement: The fatigue measurements were performed using a Precision Multiferroic Tester (Radiant Technologies, Inc.). The fatigue measurement pulse sequence consisted of a large number of triangular waveforms with a voltage amplitude large enough to completely switch the bilayer system at 1 MHz, followed by the PUND measurement (Figure S23, Supporting Information). In this measurement, the fatigue cycles were applied to the in-plane device to switch the in-plane domains as many as 3.9×10^9 cycles. The fatigue cycles were interrupted regularly by PUND measurement pulses, which monitored the variation of the remanent polarization as a function of write cycles with the known combination of pulse voltage and width. For example, 18 V and 1 ms for the state-1 on the positive side of the hysteresis loop for the bilayer heterostructures of the form 50-nm-thick top $x = 0.6$ layer and 50-nm-thick bottom $x = 0.4$ layer, and 32 V and 1 ms for state-2 to imitate the writing of various multistate polarization values after a large number of fatigue cycles. Consequently, these measurements produced $\pm P^*$, $\pm P^*_r$, $\pm \hat{P}$ and $\pm \hat{P}_r$ and $\Delta P = P^* - \hat{P}$, $\Delta P_r = P^*_r - \hat{P}_r$, $-\Delta P = -P^* - (-\hat{P})$, and $-\Delta P_r = -P^*_r - (-\hat{P}_r)$ as explained previously in the section on the PUND measurements. These four terms (ΔP, $-\Delta P$, ΔP_r, $-\Delta P_r$) defined here were four different calculations of the remanent polarization only and had again produced very similar results.

Supporting Information

Supporting Information is available from the Wiley Online Library or from the author.

Acknowledgements

P.K. and A.M.R. contributed equally to this work. P.K., P.B., J.A.Z, L.-Q.C., and L.W.M. acknowledge the support of the Army Research Office under the ETHOS MURI via cooperative agreement W911NF-21-2-0162. P.K. also acknowledges partial support of Intel Corp. via the COFEEE Program. A.M.R. acknowledges the Pennsylvania State University Graduate Fellowship and the support of the National Science Foundation Graduate Research Fellowship Program under Grant No. DGE1255832. X.H. acknowledges the support from the SRC-JUMP ASCENT center. C.-C.L. acknowledges the support of the Army Research Office under grant W911NF-21-1-0118 and the Taiwan Major Fields Scholarship from the Ministry of Education in Taiwan. L.C. acknowledges financial support from the Ford Foundation and the University of California President's Postdoctoral Fellowship Program. L.-Q.C. and L.W.M. also acknowledge partial support from the U.S. Department of Energy, Office of Science, Office of Basic Energy Sciences, under Award Number DE-SC-0012375 for the development of multilayer ferroelectric heterostructures.

Conflict of Interest

The authors declare no conflict of interest.

Data Availability Statement

Research data are not shared.

Keywords

exchange bias, exchange springs, ferroelectrics, multistate, thin films

Received: March 1, 2023
Revised: May 28, 2023
Published online: July 23, 2023

[1] Y. N. Young, M. J. Shelley, D. B. Stein, *Math. Biosci. Eng.* **2021**, *18*, 2849.
[2] T. Gao, Z. Li, *Phys. Rev. Lett.* **2017**, *119*, 108002.
[3] F. Liang, X. M. Luo, G. P. Zhang, *Mater. Sci. Eng., A* **2019**, *743*, 436.
[4] X. L. Wu, P. Jiang, L. Chen, J. F. Zhang, F. P. Yuan, Y. T. Zhu, *Mater. Res. Lett.* **2014**, *2*, 185.
[5] Y. Chu, L. W. Martin, M. B. Holcomb, M. Gajek, S. Han, Q. He, N. Balke, C. Yang, D. Lee, W. E. I. Hu, Q. Zhan, P. Yang, A. F. Iguez, A. Scholl, S. X. Wang, R. Ramesh, **2008**, *7*, 478.
[6] J. M. Hu, C. G. Duan, C. W. Nan, L. Q. Chen, *npj Comput. Mater.* **2017**, *3*, 18.
[7] W. H. Meiklejohn, C. P. Bean, *Phys. Rev.* **1956**, *102*, 1413.
[8] J. Nogués, I. K. Schuller, *J. Magn. Magn. Mater.* **1999**, *192*, 203.
[9] A. E. Berkowitz, K. Takano, *J. Magn. Magn. Mater.* **1999**, *200*, 552.
[10] R. L. Stamps, *J. Phys. D* **2000**, *33*, R247.
[11] J. ichi Fujikata, K. Ishihara, K. Hayashi, H. Yamamoto, K. Yamada, *IEEE Trans. Magn.* **1995**, *31*, 3936.
[12] L. V. Meloa, L. M. Rodrigues, P. P. Freitasa, *IEEE Trans. Magn.* **1997**, *33*, 3295.

[13] A. Bill, H. B. Braun, *J. Magn. Magn. Mater.* **2004**, *272–276*, 1266.
[14] G. Arlt, H. Neumann, *Ferroelectrics* **1988**, *87*, 109.
[15] A. R. Damodaran, E. Breckenfeld, Z. Chen, S. Lee, L. W. Martin, *Adv. Mater.* **2014**, *26*, 6341.
[16] D. Lee, B. C. Jeon, S. H. Baek, S. M. Yang, Y. J. Shin, T. H. Kim, Y. S. Kim, J. G. Yoon, C. B. Eom, T. W. Noh, *Adv. Mater.* **2012**, *24*, 6490.
[17] C. M. Folkman, S. H. Baek, C. T. Nelson, H. W. Jang, T. Tybell, X. Q. Pan, C. B. Eom, *Appl. Phys. Lett.* **2010**, *96*, 052903.
[18] J. H. Lee, N. X. Duong, M. H. Jung, H. J. Lee, A. Kim, Y. Yeo, J. Kim, G. H. Kim, B. G. Cho, J. Kim, F. U. H. Naqvi, J. S. Bae, J. Kim, C. W. Ahn, Y. M. Kim, T. K. Song, J. H. Ko, T. Y. Koo, C. Sohn, K. Park, C. H. Yang, S. M. Yang, J. H. Lee, H. Y. Jeong, T. H. Kim, Y. S. Oh, *Adv. Mater.* **2022**, *34*, 2200083.
[19] R. V. K. Mangalam, J. Karthik, A. R. Damodaran, J. C. Agar, L. W. Martin, *Adv. Mater.* **2013**, *25*, 1761.
[20] J. C. Agar, A. R. Damodaran, M. B. Okatan, J. Kacher, C. Gammer, R. K. Vasudevan, S. Pandya, L. R. Dedon, R. V. K. Mangalam, G. A. Velarde, S. Jesse, N. Balke, A. M. Minor, S. V. Kalinin, L. W. Martin, *Nat. Mater.* **2016**, *15*, 549.
[21] P. Zubko, G. Catalan, A. K. Tagantsev, *Annu. Rev. Mater. Res.* **2013**, *43*, 387.
[22] J. Karthik, R. V. K. Mangalam, J. C. Agar, L. W. Martin, *Phys. Rev. B: Condens. Matter Mater. Phys.* **2013**, *87*, 024111.
[23] J. Lee, C. H. Choi, B. H. Park, T. W. Noh, J. K. Lee, *Appl. Phys. Lett.* **1998**, *72*, 3380.
[24] P. W. M. Blom, R. M. Wolf, J. F. M. Cillessen, M. P. C. M. Krijn, *Phys. Rev. Lett.* **1994**, *73*, 2107.
[25] E. G. Lee, D. J. Wouters, G. Willems, H. E. Maes, *Appl. Phys. Lett.* **1996**, *69*, 1223.
[26] H. Lee, T. H. Kim, J. J. Patzner, H. Lu, J. W. Lee, H. Zhou, W. Chang, M. K. Mahanthappa, E. Y. Tsymbal, A. Gruverman, C. B. Eom, *Nano Lett.* **2016**, *16*, 2400.
[27] J. W. Lee, K. Eom, T. R. Paudel, B. Wang, H. Lu, H. X. Huyan, S. Lindemann, S. Ryu, H. Lee, T. H. Kim, Y. Yuan, J. A. Zorn, S. Lei, W. P. Gao, T. Tybell, V. Gopalan, X. Q. Pan, A. Gruverman, L. Q. Chen, E. Y. Tsymbal, C. B. Eom, *Nat. Commun.* **2021**, *12*, 6784.
[28] P. Wu, X. Ma, Y. Li, V. Gopalan, L. Q. Chen, *Appl. Phys. Lett.* **2012**, *100*, 092905.
[29] V. Anbusathaiah, D. Kan, F. C. Kartawidjaja, R. Mahjoub, M. A. Arredondo, S. Wicks, I. Takeuchi, J. Wang, V. Nagarajan, *Adv. Mater.* **2009**, *21*, 3497.
[30] Y. Zhang, M. G. Han, J. A. Garlow, Y. Tan, F. Xue, L. Q. Chen, P. Munroe, N. Valanoor, Y. Zhu, *Nano Lett.* **2019**, *19*, 5319.
[31] S. Matzen, O. Nesterov, G. Rispens, J. A. Heuver, M. Biegalski, H. M. Christen, B. Noheda, *Nat. Commun.* **2014**, *5*, 4415.
[32] K. P. Kelley, Y. Ren, A. N. Morozovska, E. A. Eliseev, Y. Ehara, H. Funakubo, T. Giamarchi, N. Balke, R. K. Vasudevan, Y. Cao, S. Jesse, S. V. Kalinin, *ACS Nano* **2020**, *14*, 10569.
[33] K. P. Kelley, Y. Ren, A. Dasgupta, P. Kavle, S. Jesse, R. K. Vasudevan, Y. Cao, L. W. Martin, S. V. Kalinin, *ACS Nano* **2021**, *15*, 15096.
[34] T. M. Ræder, S. Qin, R. K. Vasudevan, T. Grande, J. C. Agar, M. J. Zachman, *Adv. Sci.* **2022**, *2201530*, 2201530.
[35] P. Kavle, J. A. Zorn, A. Dasgupta, B. Wang, M. Ramesh, L. Q. Chen, L. W. Martin, *Adv. Mater.* **2022**, *34*, 2203469.
[36] A. K. Yadav, C. T. Nelson, S. L. Hsu, Z. Hong, J. D. Clarkson, C. M. Schlepuëtz, A. R. Damodaran, P. Shafer, E. Arenholz, L. R. Dedon, D. Chen, A. Vishwanath, A. M. Minor, L. Q. Chen, J. F. Scott, L. W. Martin, R. Ramesh, *Nature* **2016**, *530*, 198.
[37] L. J. McGilly, A. Schilling, J. M. Gregg, *Nano Lett.* **2010**, *10*, 4200.
[38] R. Waser, N. A. Pertsev, V. G. Koukhar, *Phys. Rev. B: Condens. Matter Mater. Phys.* **2001**, *64*, 214103.
[39] A. Jain, A. K. Panwar, A. K. Jha, *J. Mater. Sci.* **2016**, *27*, 9911.
[40] F. Xue, J. J. Wang, G. Sheng, E. Huang, Y. Cao, H. H. Huang, P. Munroe, R. Mahjoub, Y. L. Li, V. Nagarajan, L. Q. Chen, *Acta Mater.* **2013**, *61*, 2909.
[41] L. Zhou, C. Dai, P. Meisenheimer, S. Das, Y. Wu, F. Gómez-Ortiz, P. García-Fernández, Y. Huang, J. Junquera, L. Q. Chen, R. Ramesh, Z. Hong, *Adv. Funct. Mater.* **2022**, *32*, 2111392.
[42] E. E. Fullerton, J. S. Jiang, S. D. Bader, *J. Magn. Magn. Mater.* **1999**, *200*, 392.
[43] E. E. Fullerton, J. S. Jiang, M. Grimsditch, C. H. Sowers, S. D. Bader, *Phys. Rev. B* **1998**, *58*, 12193.
[44] J. P. Prieto-Ruiz, F. M. Romero, H. Prima-García, E. Coronado, *J. Mater. Chem. C* **2015**, *3*, 11122.
[45] M. Acharya, E. Banyas, M. Ramesh, Y. Jiang, A. Fernandez, A. Dasgupta, H. Ling, B. Hanrahan, K. Persson, J. B. Neaton, L. W. Martin, *Adv. Mater.* **2022**, *34*, 2105967.
[46] A. R. Damodaran, S. Pandya, Y. Qi, S. L. Hsu, S. Liu, C. Nelson, A. Dasgupta, P. Ercius, C. Ophus, L. R. Dedon, J. C. Agar, H. Lu, J. Zhang, M. Andrew, A. M. Rappe, L. W. Martin, *Nat. Commun.* **2017**, *8*, 14961.
[47] R. V. K. Mangalam, J. C. Agar, A. R. Damodaran, J. Karthik, L. W. Martin, *ACS Appl. Mater. Interfaces* **2013**, *5*, 13235.
[48] M. J. Haun, E. Furman, S. J. Jang, H. A. McKinstry, L. E. Cross, *J. Appl. Phys.* **1987**, *6*, 3331.
[49] N. Pertsev, A. Tagantsev, N. Setter, *Phys. Rev. B: Condens. Matter Mater. Phys.* **2000**, *61*, R825.
[50] Y. Ding, W. Ma, *AIP Adv.* **2020**, *10*, 015022.
[51] Y. L. Li, S. Y. Hu, Z. K. Liu, L. Q. Chen, *Appl. Phys. Lett.* **2002**, *81*, 427.
[52] X. Xing, J. Chen, J. Deng, G. Liu, *J. Alloys Compd.* **2003**, *360*, 286.
[53] R. Uecker, B. Velickov, D. Klimm, R. Bertram, M. Bernhagen, M. Rabe, M. Albrecht, R. Fornari, D. G. Schlom, *J. Cryst. Growth* **2008**, *310*, 2649.